Advances in Science and Technology Research Journal

Advances in Science and Technology Research Journal, 2026, 20(7), 17–32
https://doi.org/10.12913/22998624/218033
ISSN 2299-8624, License CC-BY 4.0

Received: 2026.01.07
Accepted: 2026.05.15
Published: 2026.06.01

Service life of perforated sifting plates with holes of complex geometry under technological load

Serhii Kharchenko[1,2*], Sylwester Samborski[1], Paweł Droździel[1], Jakub Paśnik[1]

[1] Department of Fundamentals of Production Engineering, Lublin University of Technology, ul. Nadbystrzycka 38D, 20-618 Lublin, Poland
[2] Poltava State Agrarian University, 1/3 Skovorody Str., Poltava, 36003, Ukraine
* Corresponding author's e-mail: s.kharchenko@pollub.pl

ABSTRACT

The structural reliability of perforated sifting plates operating under dynamic loading conditions, including vibration, is a subject of growing scientific interest in the development of advanced material separation technologies. Although the use of perforated plates with non-standard or complex-shaped holes enhances sifting efficiency, it also introduces geometric features that may affect fatigue life and mechanical strength. This study proposes an integrated experimental–numerical methodology for predicting the service life of such perforated plates. The research involves abrasive wear testing of steel plates, characterization of loose materials (wheat, corn, granite), and finite element analysis of stress concentration zones using ABAQUS. Stress concentration factors were calculated for various critical regions of the perforated plate, considering geometric modifications, abrasive wear progression, and distributed mechanical loading. The modeling results were cross-validated with physical wear measurements obtained from real operating conditions. The methodology enables the evaluation of strength conditions and the estimation of fatigue durability under variable loading and material loss. The findings provide a basis for the optimized design, maintenance, and lifetime prediction of perforated sifting plates with complex geometries.

Keywords: perforated plate, loose material, stress concentration, reliability, durability, service life, fatigue limit, finite element analysis.

INTRODUCTION

Perforated plates are widely used as functional elements in technological equipment [1], including separation machines designed to classify granular materials based on particle size [2]. To enhance the efficiency of the separation process, mechanical vibration is often employed, which improves the dynamic properties of the granular medium and facilitates particle segregation within the material layer [3].

The successful implementation of perforated sifting plates with complex geometry (CG) holes has demonstrated their technological feasibility and potential. [4,5]. These holes are designed to align with the geometric deviations of the majority of particle shapes found in loose materials, thereby increasing the throughput rate per unit time without additional energy consumption. As a result, a higher specific productivity and reduced energy consumption of the separation process are achieved [6].

Despite these advantages, the reliability aspects of such perforated plates, especially those with geometrically complex hole shapes, remain insufficiently understood.

Under external loading conditions, whether due to material weight or vibrations, stress concentrations inevitably arise in their structures [7]. The structural integrity of a perforated plate is influenced by the formation of stress concentrators, which typically develop in the ligament regions between adjacent holes [8]. This confirms the stress distribution in perforated plates with round holes of different thicknesses, which was thoroughly studied in [9].

Finite element method (FEM) is often employed to evaluate the structural integrity of perforated plates [10,11]. FEM allows accurate determination of natural vibration frequencies [12–15], critical stress values, and stress concentration zones [11,16].

Foundational analytical expressions for stress and vibration analysis of perforated structures are provided in classic works such as [17]. In [1], the combination of FEM with experimental holographic interferometry was successfully used to study deflections and stress patterns in bent perforated plates.

Discrete Element Method (DEM) has been increasingly employed to analyze the technological efficiency of separation processes and their impact on the wear characteristics of perforated plates [18]. However, the accuracy of DEM-based simulations strongly depends on extensive preliminary experimental calibration, particularly with respect to contact parameters, friction coefficients, restitution properties, and particle–wall interaction laws. Recent studies demonstrate that, in order to obtain reliable DEM predictions of separation efficiency and wear-related phenomena, calibration is required that takes into account experimentally measured physical and mechanical properties of bulk materials, including particle size distribution, density, moisture content, and interparticle friction [19, 20].

The successful application of numerical modelling to study the reliability of perforated plates, including the justification of boundary and initial conditions and the variation of perforation parameters, was described in [21]. The combined use of FEM and experimental data has proven effective in analyzing the influence of external loads on the reliability of perforated plates [22, 23].

To date, most studies have primarily focused on plates with standard hole geometries, such as circular [10, 11], rectangular [24], and various other shapes, including semi-circular, elliptical, square, triangular, and rhombic [25, 26]. Studies have shown that circular holes offer the most favorable stress distribution, with the lowest stress concentration factors compared to shapes with sharp corners [27].

One of the most influential factors affecting the reliability of perforated plates is their thickness [13]. In [25], the authors proposed modeling the holes as areas of negligible thickness within the plate, leading to a heterogeneous thickness profile. This approach can provide the necessary reliability metric predictions under certain modeling conditions and refinement experiments.

In practical applications involving vibrating plates, additional external loads are introduced by the layer of loose material resting on the perforated plate. This load depends on the material's loose density and the thickness of the layer. It contributes to elevated internal stresses that may lead to structural deformation.

Another detrimental factor is the progressive reduction in plate thickness due to abrasive mechanical wear during operation [26–28]. This wear-induced thickness reduction leads to a corresponding decline in flexural stiffness, which is proportional to the cube of the plate's thickness and also depends on the Young's modulus and Poisson's ratio.

The aim of this study is to develop a methodology for predicting the service life of perforated screening plates with complex geometry holes, based on experiments and FEM simulations, taking into account the geometric parameters of the plates and the abrasive properties/distributed load from loose material.

MATERIALS AND STUDY OBJECTS

The critical stresses arising in perforated plate are determined by a combination of factors, including the degree of thickness reduction due to abrasive wear, the magnitude of external loads from loose materials, and the geometric characteristics of the perforations.

Optimization of geometric parameters with respect to the critical stress criterion is essential for maximizing the operational lifespan of sifting plates with geometrically complex holes. Three design solutions for holes with complex geometry (Figure 1) were selected for research: a 5-fold epicycloid (k = 5), a 7-fold epicycloid (k = 7), and a 9-fold epicycloid (k = 9).

Given the technological advantages associated with epicycloidal hole geometries and the insights from prior studies [13, 31], a set of representative geometric and material parameters was selected for this study (Table 1).

The selected range of plate thickness (0.6–1.0 mm) is based on the anticipated reduction of initial thickness (1.0 mm) by up to 40% due to wear. The chosen values for hole geometry and ligament width were determined with reference to established experimental findings [13, 31].

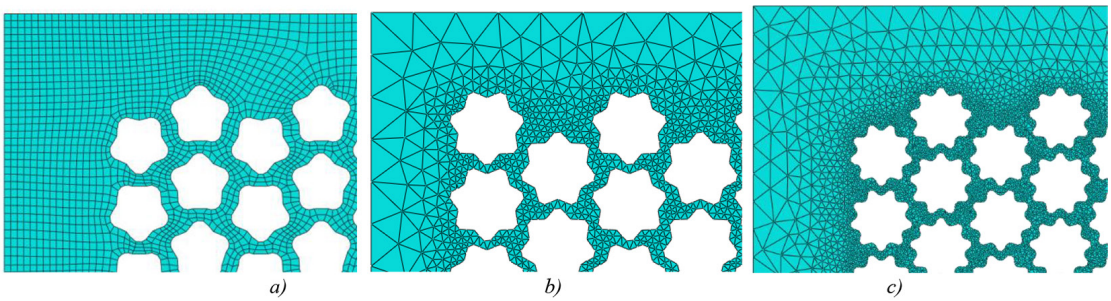

a) b) c)

Figure 1. Investigated perforated plates with epicycloidal-shaped holes and varying configurations: a) k = 5, b) k = 7, c) k = 9

Table 1. Parameters of investigated perforated plates

Technological indicators	Value
Material	Steel S 235 JR
Plate thickness, mm	0.6–1.0
Overall dimensions, mm	1000 × 1000
Separation radius of hole, mm	7
Epicycloid modulus (*k*)	5, 7, 9
Ligament thickness between holes, mm	1, 2, 3

To validate the simulation outcomes and ensure broader applicability of the results, three loose materials with distinct physical properties were selected for experimental study: wheat, corn and granite (Figure 2).

METHODOLOGY

To determine the service life of perforated plates before the onset of structural deformation, a comprehensive methodology was used in the study, which includes experimental methods and numerical (FEM) modelling. The proposed algorithm includes four main stages: experimental determination of wear intensity, determination of the properties of loose material, development of an FEM model, and analysis of the results.

In the first stage, the abrasive wear intensity of the perforated plates under operational conditions was experimentally evaluated. Abrasive interaction with loose material leads to a reduction in plate thickness over time, which negatively affects the plate's stiffness and structural integrity. The second stage involved experimental determination of the distributed loading exerted by the loose material on the perforated plate. These loads were evaluated based on material density, layer thickness, and particle behavior during vibration-assisted separation. The third stage involved FEM-based numerical modeling to identify critical stress concentrations within the perforated plate under varying loading and geometric conditions. The numerical model accounted for variable plate thickness resulting from progressive wear, complex hole geometry, and spatially distributed external loading. The structural integrity was assessed by comparing the actual stress obtained from FEM with the allowable stress, according to the following condition [32, 33]:

$$\sigma \leq [\sigma] \tag{1}$$

where: σ is the von Mises stress from FEM; $\sigma = R_e/n_s$ – allowable stress; R_e is the yield strength; n_s is safety factor, determined based on standard engineering design practices, $n_s = 1 – 1.7$ [33].

a) b) c)

Figure 2. Samples of loose materials used in experiments: a) wheat, b) corn, c) granite

Integrating experimental data into the FEM model will allow identifying areas on the plate with high stresses and assessing structural limits under real operating conditions. The methodology was verified by comparing simulated stress values with material limits and analyzing deformation patterns.

Numerical modelling (FEM)

FEM of perforated plates was performed using the Abaqus/CAE 2018 software package, following a structured simulation workflow that included the following modules (Figure 3): Part – creation of the 3D geometry of the perforated plate, including epicycloidal holes; Property – assignment of material properties; Step – definition of analysis steps and procedures; Interaction – definition of contact interactions and constraints; Load – application of distributed load and boundary conditions; Mesh – generation of the finite element mesh; Job – submission and execution of the analysis; Visualization – post-processing and result analysis. Material properties used for the steel perforated plates are summarized in Table 2.

The loose materials used in the experimental study were characterized not only by their

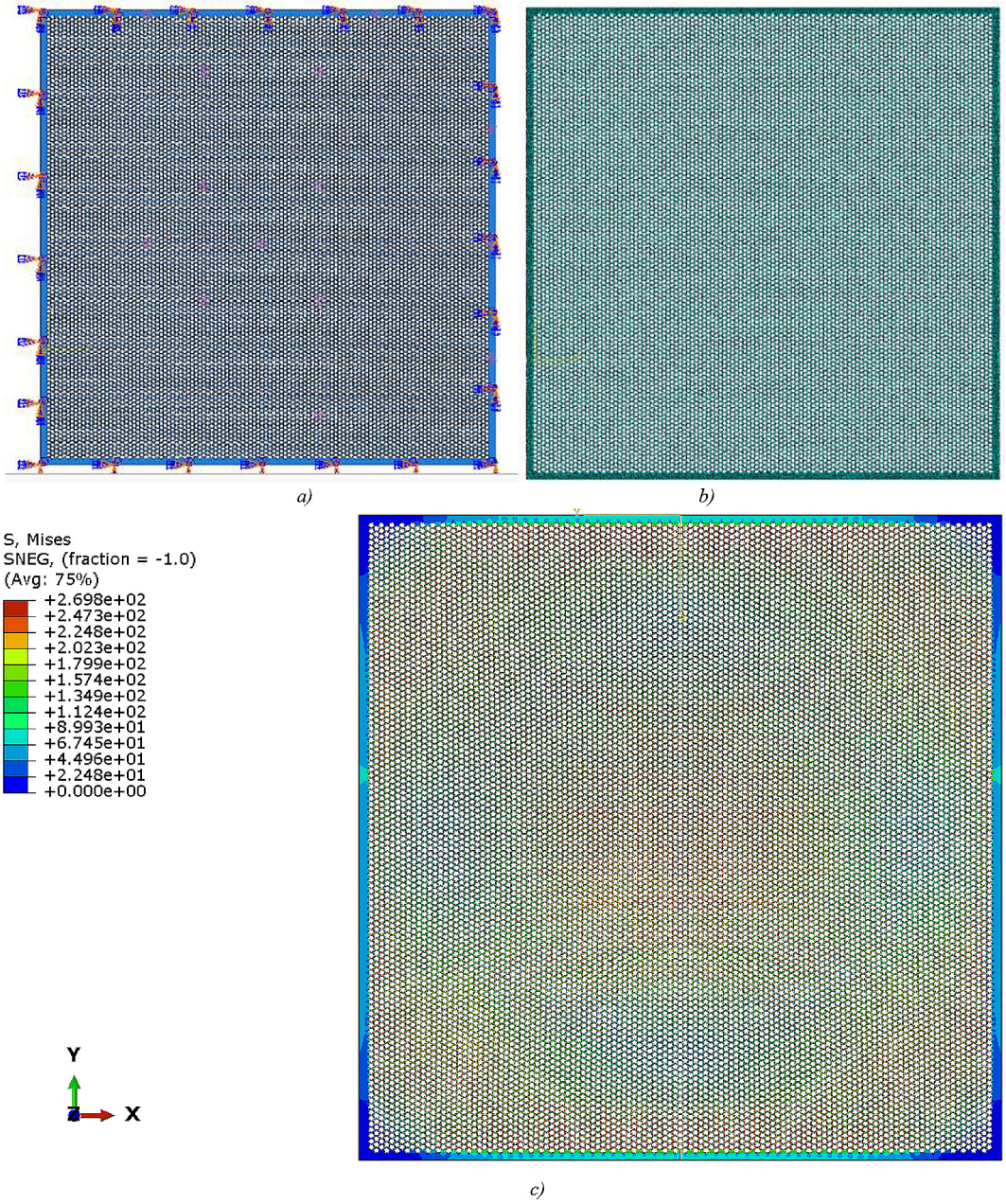

Figure 3. FEM modeling stages for a perforated plate: a) load, b) mesh, c) vizualization

Table 2. Material properties of the perforated steel plate

Properties	Unit	Value
Young's modulus *E*	GPa	207
Mass density ρ	kg/m^3	7800
Poisson's ratio *v*	-	0.3
Yield strength σ_t	MPa	235
Ultimate tensile strength	MPa	360
Elongation at break	%	26

type but also by selected physical properties known to influence particle–structure interaction. For cereal grains (wheat and corn), representative ranges of characteristic dimensions (length, width, and thickness) and moisture content (W=14%) were considered. Granite was considered to be an unchanging, non-deformable abrasive material with high hardness, independent of moisture content. Well-known studies demonstrate that moisture content significantly affects grain size and mechanical properties, thereby influencing contact forces and motion characteristics in both experimental observations and DEM-based simulations [34, 35]. To capture the effects of geometric and material variables, a full-factorial design of 27 FEM models was developed. The following parameters were varied: hole geometry with different epicycloid modulus; ligament width between holes; plate thickness, loose material type. The model matrix is detailed in Table 3: epicycloid modulus, ligament width, type of loose material, plate thickness (mm).

The positive experience with Abaqus/CAE 2018 for static and dynamic simulation of perforated plates has been reported in several prior works [12, 13, 36], confirming its suitability for detailed structural stress analysis under distributed loads and vibrational conditions.

Each finite element model was discretized using triangular shell elements S3 type, with an average mesh density of 850000–2730000 elements per model, depending on the hole geometry and ligament width. Local mesh refinement was applied in the vicinity of perforation edges and ligament regions to accurately capture stress gradients, while a coarser mesh was used in low-gradient areas to reduce computational cost. Additional mesh refinement tests confirmed that increasing the mesh density beyond this level resulted in less than 1% change in stress results, indicating mesh independence and reliability of the simulation results.

Table 3. Investigated parameters for FEM models

Model No	Epicycloid modulus *k*	Ligament width *a*, mm	Type of loose material	Plate thickness *s*, mm	Model No	Epicycloid modulus *k*	Ligament width *a*, mm	Type of loose material	Plate thickness *s*, mm
1	5	1	wheat	0.6	19	9	1	granite	0.6
2				0.8	20				0.8
3				1	21				1
4		2		0.6	22		2		0.6
5				0.8	23				0.8
6				1	24				1
7		3		0.6	25		3		0.6
8				0.8	26				0.8
9				1	27				1
10	7	1	corn	0.6					
11				0.8					
12				1					
13		2		0.6					
14				0.8					
15				1					
16		3		0.6					
17				0.8					
18				1					

Experimental studies

The structural reliability of a perforated plate is strongly dependent on its flexural rigidity, defined as: $D = \frac{Es^3}{12(1-\nu^2)}$, where E – modulus of elasticity, s – plate thickness, ν – Poisson's ratio [13]. Since rigidity is proportional to the cube of the plate thickness, accurate representation of the residual thickness during operation is critical for reliable FEM simulations [13].

To determine the actual thickness reduction during operation, in situ measurements were conducted under industrial conditions. A Mitutoyo 389–514 digital micrometer for thin plate measurement was used, with specifications: measuring range 0–25.4 mm; resolution 4 µm; maximum reach 330 mm. Thickness measurements were taken at intervals of 100 mm across the plate surface. Average values were calculated from multiple sampling points to quantify wear over time.

The experimentally measured thickness loss of the perforated plate is denoted by $\delta(t)$. The instantaneous wear rate is defined as [30]:

$$\gamma(t) = \frac{d\delta(t)}{dt} \tag{2}$$

where: δ – thickness of the worn layer of the plate material; t – operating time.

Friction between loose material particles and the perforated plate also influences the wear rate and intensity. Additionally, the properties of loose material that define the magnitude of the external load on the perforated plates were determined experimentally. Under production conditions, the average thickness of the loose material layer moving across the perforated plate was measured. Also, using a calibrated measuring container, the average density of the loose material was established.

For further use as a distributed load, the pressure exerted by the material on the plate surface was calculated. Technologically, during sifting, a portion of the loose material (typically up to 30%) passes through the holes, while the remainder stays on the perforated plate surface.

It is assumed that the layer height decreases linearly along the perforated plate [37]:

$$h_m(x) = h_{m0}\left(1 - \alpha\frac{x}{L}\right) \tag{3}$$

where: $h_m(x)$ is the layer height at distance $x \in [0, L]$; h_{m0} is the initial height of the loose material layer; α is the dimensionless fraction of material passing through the perforations (0–1); L is the plate length.

In this study, the throughput fraction was set to $\alpha = 0.20$, which corresponds to a stable operating regime in which a limited portion of the feed passes through the perforations while the remaining fraction is transported along the plate surface. The mean layer thickness was taken as $h_m = 30$ mm based on in situ observations of the material bed during continuous operation and was used as a representative average value to enable consistent comparison across the investigated loose materials. The instantaneous distributed pressure (load per area) is then:

$$q(x) = \rho g h_m(x) = \rho g h_{m0}\left(1 - \alpha\frac{x}{L}\right) \tag{4}$$

where: g – gravitational acceleration; ρ – density of loose material.

For simplification, the average distributed pressure along the plate is calculated as:

$$\bar{q} = \frac{1}{L}\int_0^L q(x)dx = \rho g h_{m0}\left(1 - \frac{\alpha}{2}\right) \tag{5}$$

where: assuming $L = 1$ m.

Within Equations 3–5, both α and h_m directly control the local layer height $h(x)$ and, consequently, the distributed pressure q. To ensure consistency between experimental observations and analytical modelling, the wear coefficient is introduced in an operational, time-dependent form:

$$k_w(t) = \frac{1}{F_f}\frac{d\delta(t)}{dt} \tag{6}$$

where: $F_f = \mu N$ – friction force [38], μ – frictional coefficient of loose material; N – applied normal force.

The friction coefficients for wheat, corn, and granite on a steel surface were experimentally determined using the methodology from [39].

This formulation reflects the instantaneous intensity of abrasive wear under given operating conditions. For engineering evaluations and comparison of different loose materials, an average operational wear coefficient is introduced over a time interval T:

$$k_w(t) = \frac{\delta(T) - \delta(0)}{F_f T} \tag{7}$$

The wear coefficient (in µm/(N·h)) accounts for the abrasive properties of the environment and technological conditions and is useful for analyzing the operational service life of components.

ANALYSIS OF RESULTS AND DISCUSSION

Experimental data

The properties of the studied loose materials were established, and the following parameters were determined: distributed pressure, friction force, and wear coefficient (Table 4).

The adopted values $\alpha = 0.20$ and $h_m = 30$ mm represent nominal industrial operating conditions. Since q is proportional to the height of the material layer, any increase in α and/or h_m will proportionally increase the effective load and, as a result, reduce the predicted service life. As a result of measuring the thickness reduction of the perforated plate during operation, the data shown in Table 5 were obtained.

The average operational wear coefficient listed in Table 4 was calculated according to Equation 7 using the experimentally determined average wear rates (Table 5) and friction forces. For practical application, the data are presented using quadratic polynomial equations for the given loose materials:

$$\delta(t)_{wheat} = 6.25 \times 10^{-7} t^2 + 0.01375t \quad (8)$$

$$\delta(t)_{corn} = 8.04 \times 10^{-7} t^2 + 0.0253\, t + 0.429 \quad (9)$$

$$\delta(t)_{granite} = 14.29 \times 10^{-7}\, t^2 + 0.0481\, t + 1.429 \quad (10)$$

where: $\delta(t)$ –thickness reduction, t – operating time.

Analysis of the wear kinetics in Table 5 confirms a pronounced nonlinear trend for all materials, with a gradual increase in the interval wear rate over time. For wheat, the incremental wear rate rises from 0.015 µm/h (0–2000 h) to 0.0225 µm/h (6000–8000 h), while for corn it increases from 0.0275 µm/h to 0.0375 µm/h over the same intervals. The most severe acceleration is observed for granite, where the rate increases from 0.0525 µm/h (0–2000 h) to 0.0725 µm/h (6000–8000 h). In terms of cumulative thickness loss at 8000 h, granite exhibits 480 µm compared to 150 µm for wheat and 255 µm for corn, i.e., approximately 220% and 88% higher, respectively. Importantly, the first signs of plastic deformation were observed after 6000 h of operation, particularly during granite screening, which corresponds to a thickness loss of 335 µm (≈33.5% of the initial 1.0 mm plate thickness) and indicates an approaching critical stiffness reduction. Considering this, the range of perforated plate thicknesses used for numerical modeling was 0.6–1.0 mm.

FEM data

The numerical modeling provided stress distribution in perforated plates under different conditions. The zones with the highest stress levels

Table 4. Properties of loose material

Properties	Type of loose material		
	wheat	corn	granite
Layer thickness h_m, mm	30	30	30
Average density ρ, kg/m³	780	750	1600
Friction coefficient µ	0.4	0.35	0.6
Through fraction α	0.20		
Friction force F_r, N	100	67.2	253.2
Wear coefficient, µm/(N·h)	0.00019	0.00048	0.00024
Distributed pressure q, Pa	250	192	422

Table 5. Wear parameters of the perforated plate

Type of loose material	Thickness reduction of perforated plate $\delta\delta$, µm					Average wear rate, µm/h
	Operating time, hours					
	0	2000	4000	6000	8000	
wheat	0	30	65	105	150	0.019
corn	0	55	115	180	255	0.032
granite	0	105	220	335	480	0.06

were identified: peripheral (*A*) and central (*B*) (Figure 4). Zone A was defined as the peripheral strip adjacent to the clamped boundary, spanning the first four rows of perforations and ligaments measured inward from the plate edge (resulting in an effective width of approximately 0.10–0.12 m for the considered layouts). Zone B was defined as the remaining central perforated region after excluding Zone A. Both regions were implemented as element sets in Abaqus/CAE to ensure identical spatial sampling across models.

Regardless of the loose material type, hole geometry, or plate thickness, these zones were consistently observed. Thus, the subsequent analysis focused on maximum stress values specifically in these zones, where deformation is most likely to occur.

During the finite element analysis of perforated thin-walled plates subjected to distributed loading, extremely high local von Mises stresses were observed at the edges of perforations and within narrow ligaments between adjacent holes (Table 6, Figure 5). Such stress peaks were most pronounced for small ligament widths and in regions adjacent to the clamped peripheral boundary. This behavior was attributed to the presence of stress singularities, which naturally arise in linear elastic formulations when the structural geometry includes sharp curvature transitions, closely spaced openings, or abrupt boundary constraints. From the standpoint of continuum mechanics, these singularities are associated with locally unbounded stress gradients and do not correspond to a physically realizable average stress state within a finite material volume. Similar observations and interpretations have been widely reported in studies on notched and perforated components [22, 40].

From the finite element methodology perspective, the maximum von Mises stresses $\sigma_{vM}^{\max}$ were found to be mesh-dependent and increased with local mesh refinement, which is a classical indicator of singular behavior [41]. Therefore, these peak values were interpreted not as quantitative measures of the global structural response, but rather as qualitative indicators of potential locations for damage initiation, such as local yielding, microcrack formation, or accelerated wear. Direct comparison of $\sigma_{vM}^{\max}$ with material strength limits was thus considered methodologically unjustified, in accordance with established recommendations for FEM-based stress assessment [42].

To obtain physically meaningful and mesh-independent stress measures, an averaging approach was implemented. Two critical regions were defined:

- Zone *A*, located near the clamped peripheral boundary;
- Zone *B*, located in the central part of the perforated plate.

The local von Mises stress field $\sigma_{vM}(x)$ was extracted in Abaqus/CAE using the command sequence: *Visualization* → *Field Output* → *Variable: S* → *Invariant: Mises*, with Position = Integration Point to avoid nodal extrapolation effects [43]. For Zone A, an element set including four rows of perforations and ligaments adjacent to the plate edge was selected, corresponding to a peripheral

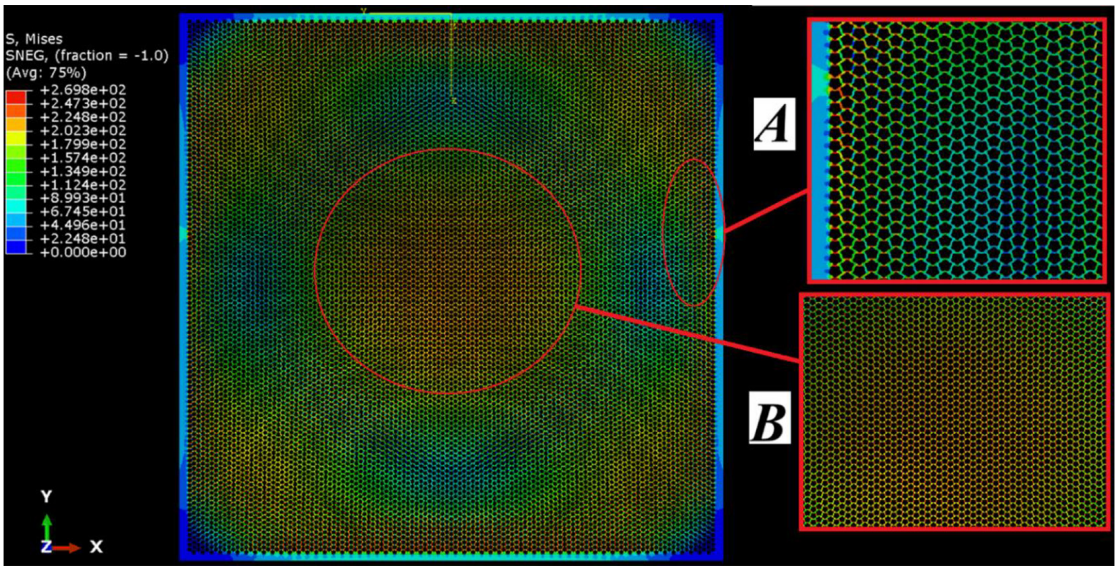

Figure 4. Zones of maximum stress in the perforated plate

Table 6. Maximum stresses in a perforated plate with epicycloidal holes (type of loose material – wheat; ligament width a = 1 mm)

Model No	Plate thickness, mm	Modulus epicycloid k = 5		Modulus epicycloid k = 7		Modulus epicycloid k = 9	
		Stresses in the zone A σ_{AvM}^{max}, MPa	Stresses in the zone B σ_{BvM}^{max}, MPa	Stresses in the zone A σ_{AvM}^{max}, MPa	Stresses in the zone B σ_{BvM}^{max}, MPa	Stresses in the zone A σ_{AvM}^{max}, MPa	Stresses in the zone B, MPa
1	0.6	440.8	157.4	586.7	244.5	658.9	274.6
2	0.8	249	88.9	334.7	139.4	382.7	159.5
3	1	160	57.2	217.6	90.6	252.9	105.4

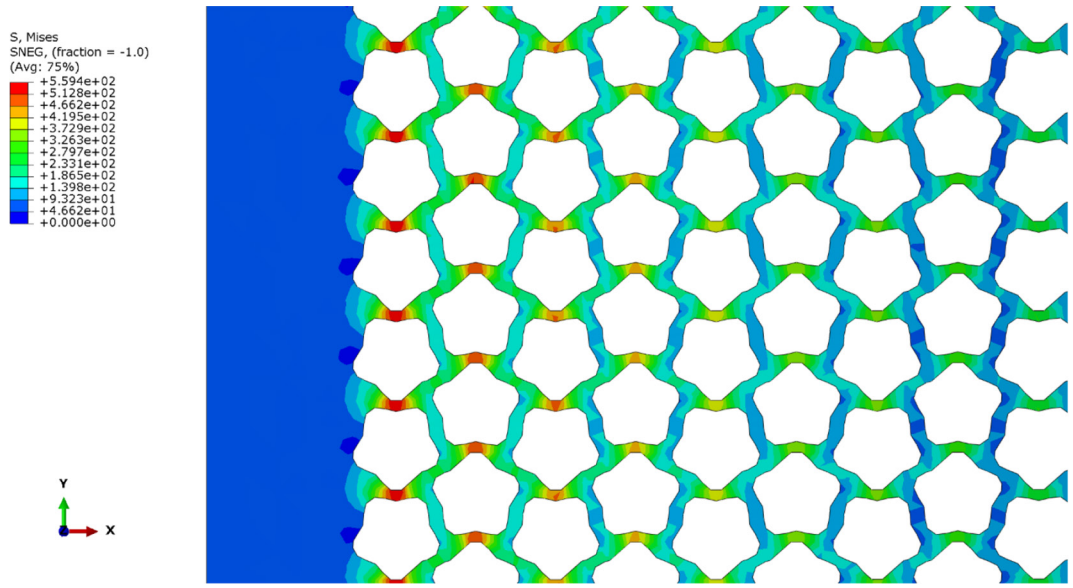

Figure 5. Visualization of maximum stresses in the peripheral zone of a perforated plate under external loading

strip of about 0.10–0.12 m in width. Given the total plate size of 1 m × 1 m, the area of Zone A was therefore estimated as $S_{\Omega,A}$ = 0.3 m^2. Zone B was defined as the remaining central region, excluding the peripheral strip, with an estimated area of $S_{\Omega,B}$ = 0.45 m^2. These dimensions ensured that each zone contained a sufficiently large number of finite elements and perforation units to provide statistically representative stress measures.

The area-averaged von Mises stress was then evaluated according to

$$\bar{\sigma}_{vM} = \frac{1}{S_\Omega}\int_\Omega \sigma_{vM}(x)\,dS, \Omega \in \{\text{Zone A, Zone B}\} \quad (11)$$

where: $\sigma_{vM}(x)$ denotes the local stress field obtained from the FEM solution and S_Ω is the area of the corresponding zone.

The maximum stress σ_{vM}^{max} was retained only as an auxiliary indicator of local stress amplification due to geometric singularities, while the averaged stress $\bar{\sigma}_{vM}$ was adopted as the primary quantitative measure. The ratio $\frac{\bar{\sigma}_{vM}}{\sigma_{vM}^{max}}$ consistently remained well below unity, confirming that the extreme peak stresses were confined to very small regions and did not govern the global stress state.

The averaged stresses exhibited stable convergence with mesh refinement and revealed clear, physically consistent trends with respect to plate thickness, ligament width, and perforation geometry. Consequently, these values were reported in the tabulated results (Table 7) and used as the basis for comparative analysis, while the maximum stresses were discussed exclusively in the context of local stress concentration and potential damage initiation, following established FEM practice [40, 41].

Table 7 systematizes the key physical and tribological parameters of the investigated loose materials and quantitatively explains their different impacts on the durability of perforated sifting plates. An increase in loose density and friction coefficient from wheat to corn and further to granite resulted in a pronounced rise of the effective distributed load acting on the sieve,

which was reflected in the growth of the calculated normal pressure and friction force. As a consequence, the experimentally measured wear rate increased from 0.019 μm/h for wheat to 0.032 μm/h for corn and reached 0.06 μm/h for granite, i.e., granite caused more than a threefold increase in wear intensity compared with wheat (Table 4, 5). These results demonstrate a consistent correlation between material properties, operational loading, and degradation kinetics of the sifting plate. Thus, Table 7 provides a physically grounded basis for coupling experimental wear data with FEM-predicted stress states and enables reliable material-specific forecasting of sieve service life.

The influence of hole type or epicycloid module also affected stress levels in the perforated plate (Figure 6).

Figure 6 consistently demonstrated that the averaged von Mises stress in the critical peripheral zone (Zone A) decreased with increasing ligament width a for both wheat and granite at s = 0.6 mm, while the absolute stress level scaled strongly with the granular loading severity. For loose material, increasing a from 1 to 3 mm reduced $\bar{\sigma}_{vM}$ by 22.6–23.2% for k = 7, by 22.4–23.2% for k = 5, and by 21.6–22.7% for k = 9. This cross-material consistency indicates that ligament width controlled the stress concentration pathway, whereas the material type

Table 7. Averaged stresses in a perforated plate with epicycloidal holes

Model No	Ligament width a, mm	Type of loose material	Plate thickness s, mm	Modulus epicycloid k = 5		Modulus epicycloid k = 7		Modulus epicycloid k = 9	
				Averaged stresses in the zone A $\bar{\sigma}_{AvM}$, MPa	Averaged stresses in the zone B $\bar{\sigma}_{BvM}$, MPa	Averaged stresses in the zone A $\bar{\sigma}_{AvM}$, MPa	Averaged stresses in the zone B $\bar{\sigma}_{BvM}$, MPa	Averaged stresses in the zone A $\bar{\sigma}_{A}$, MPa	Averaged stresses in the zone B $\bar{\sigma}_{B}$, MPa
1	1	wheat	0.6	167.5	59.8	222.9	92.9	250.4	104.3
2			0.8	94.6	33.8	127.2	53	145.4	60.6
3			1	60.8	21.7	82.7	34.4	96.1	40.1
4	2		0.6	148.1	52.9	185.9	77.5	207.5	86.5
5			0.8	82.9	29.6	104.5	43.5	116.8	48.7
6			1	52.9	18.9	67.1	28	75.3	31.4
7	3		0.6	128.7	45.9	171.3	71.4	193.6	80.6
8			0.8	71.2	25.4	95.7	39.9	109.2	45.5
9			1	44.9	16.1	61.1	25.5	70.3	29.3
10	1	corn	0.6	128.6	45.9	171.2	71.3	192.3	80.1
11			0.8	72.7	26	97.7	40.7	111.7	46.5
12			1	46.7	16.6	63.5	26.6	73.8	30.7
13	2		0.6	113.7	40.6	142.8	59.5	159.4	66.4
14			0.8	63.7	22.7	80.3	33.5	89.7	37.4
15			1	40.6	14.5	51.5	21.5	57.8	24.1
16	3		0.6	98.8	35.3	131.6	54.8	148.7	61.9
17			0.8	54.7	19.5	73.5	30.6	83.9	34.9
18			1	34.5	12.3	46.9	19.6	54	22.5
19	1	granite	0.6	282.7	101	376.4	156.8	422.6	176.1
20			0.8	159.7	66.5	214.7	89.5	245.5	102.3
21			1	102.6	36.7	139.5	58.1	162.2	67.6
22	2		0.6	250	89.3	313.8	130.8	350.3	146
23			0.8	139.9	58.3	176.5	73.5	197.2	82.2
24			1	89.2	31.9	113.2	47.2	127.1	52.9
25	3		0.6	217.2	77.6	289.2	120.5	326.7	136.2
26			0.8	120.2	50.1	161.6	67.3	184.3	76.8
27			1	75.9	27.1	103.1	43	118.7	49.4

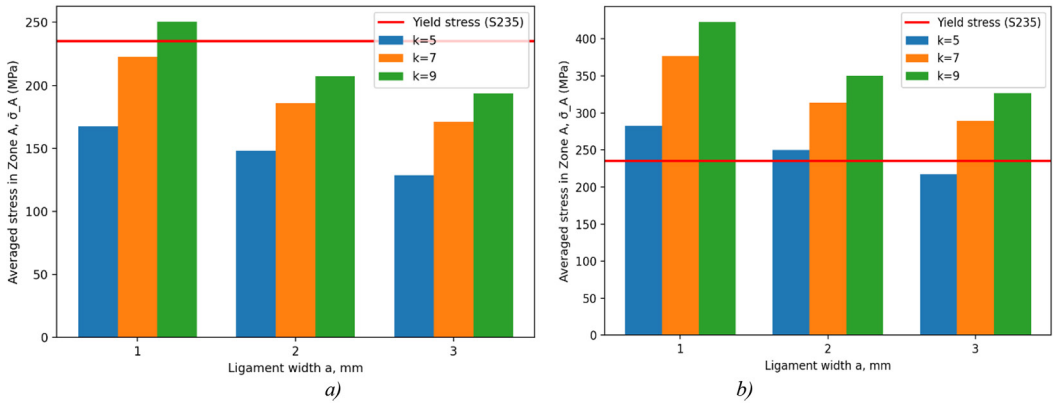

Figure 6. Dependence of average stresses (zone *A*) in a perforated plate on the ligament width and the epicycloid modulus: a) wheat loose material; b) granite loose material (s = 0.6 mm, the red line shows the permissible stress of the material [σ] = 235 MPa)

primarily controlled the loading magnitude, in line with well-established FEM observations that peak/critical stresses in perforated plates localize around ligaments and hole boundaries and scale with applied load [22].

The stress–ligament width relationship for all materials (Figure 6) was well approximated by a power-law regression (log–log fit): $\bar{\sigma}_{AvM}(a) = C\,a^{-n}$, with n ≈ 0.23–0.24 and excellent fit quality (R^2 ≈ 0.97–0.996) for the shown datasets. This form is physically consistent with the fact that ligament widening increases the effective load-carrying section and reduces stress gradients around adjacent openings. The influence of epicycloid mode k was also systematic: at a = 1 mm (wheat), increasing k from 5 to 9 increased $\bar{\sigma}_{AvM}$ by 49.5% (167.5 → 250.4 MPa). Under granite, the same increase produced 49.5% (282.7 → 422.6 MPa). These results indicate that k acted as a secondary geometric amplifier superimposed on the dominant ligament effect, while the granite case exceeded the yield threshold by a wide margin (e.g., 422.6 MPa ≈ +80% above 235 MPa), implying elastic–plastic transition under the assumed steel grade (S235) [22].

Figure 7 showed a bending-dominated thickness sensitivity: for wheat at a = 1 mm and k = 9, increasing thickness from s = 0.6 to 1.0 mm reduced $\bar{\sigma}_{AvM}$ by 61.6% (250.4→96.1 MPa). The stress–thickness dependence was accurately captured by: $\bar{\sigma}_{AvM}(s) = C_s\,s^{-m}$, m ≈ 1.88 (R^2 ≈ 0.99), which is consistent with plate bending mechanics (stress scaling strongly with thickness) and with FEM studies reporting systematic stress/SCF reduction with increasing thickness in perforated/holed plates [44, 45].

Figure 8 quantitatively confirmed the dominance of the peripheral zone: for the critical case (a = 1 mm, s = 0.6 mm, k = 9), Zone A stresses were consistently about (2.4–2.6)×Zone *B* (i.e., ~140-149%

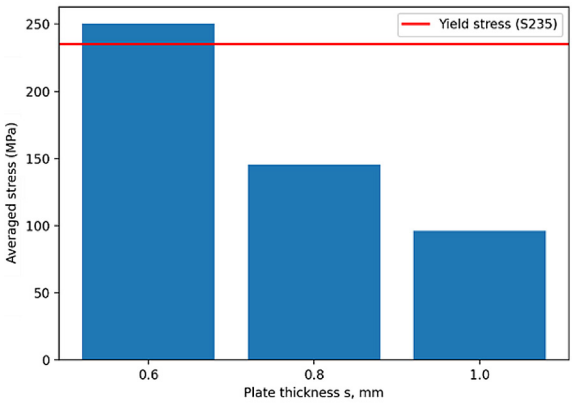

Figure 7. Dependence of average stresses (zone *A*) in a perforated plate on its thickness (wheat loose material; a = 1 mm, k = 9)

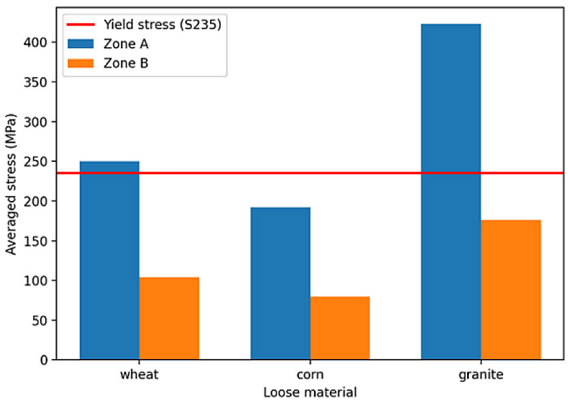

Figure 8. Changes in average stresses in different areas of a perforated plate for different loose materials (a = 1 mm, s = 0.6 mm, k = 9)

higher) for wheat, corn, and granite. This behavior is expected under clamped boundaries where bending moments and constraint effects intensify near the periphery. The granular material type produced large scaling: replacing wheat by granite increased $\bar{\sigma}_{AvM}$ by 68.8% (250.4 → 422.6 MPa). Similar trends, stress intensification around perforations and strong dependence of stress levels on load magnitude and plate details, have been reported for perforated plates under external loading and in experimental–numerical comparisons [32]. To justify factor significance quantitatively, the study used two complementary sensitivity metrics commonly applied to FEM-driven design studies [46]:

1. Local "one-factor-at-a-time" relative effect index (directly supported by the plotted controlled comparisons):

$$I_X = \frac{\sigma(X_{\max}) - \sigma(X_{\min})}{\sigma(X_{\min})} \times 100\% \qquad (12)$$

where: $X \in \{s, a, k, \text{material}\}$, and all other factors were fixed at the plotted reference conditions.

This index yields directly interpretable "engineering significance" and is frequently used in FE-based parametric sensitivity discussions [46, 47].

2. ANOVA / factorial-design effect size (variance contribution) for the multi-factor dataset:

$$\eta_X^2 = \frac{SS_X}{SS_T} = \frac{\sum_j n_j(\bar{\sigma}_j - \bar{\sigma})^2}{\sum_{i=1}^{N}(\sigma_i - \bar{\sigma})^2} \qquad (13)$$

where: SS_X is the sum of squares associated with factor X, SS_T is the total sum of squares, and n_j and $\bar{\sigma}_j$ denote the number of cases and mean stress at factor level j.

This is the standard pathway to rank factor importance in simulation-based design and is widely documented in structural design sensitivity analysis literature and factorial-design sensitivity frameworks [46, 47].

Using the relative effect index I_X computed from the most critical controlled comparisons shown in Figures 6–8, Table 7, the factors were ranked (largest-to-smallest influence on $\bar{\sigma}_{AvM}$) as granular material properties (via effective pressure and friction) (~68.8%), plate thickness s (~61.6%), epicycloid mode k (up to ~49.5% at fixed a and s), and ligament width a (~22–23%). The ranking is physically consistent: s governs bending stiffness and stress scaling; material properties govern the applied distributed load and tangential interaction; k modifies geometric stress paths; and a controls local ligament cross-section and stress gradients [22, 44, 46].

To provide a statistically grounded assessment of factor importance, an analysis of variance (ANOVA) was performed using the averaged von Mises stresses in Zone *A* for the critical configuration ($k = 9$), derived directly from the numerical data presented in the table. The factors considered were: plate thickness (s), ligament width (a), and type of loose material. Based on the computed values from the dataset (27 cases in Table 7), the following results were obtained: plate thickness (s): $\eta_s^2 = 0.52$ (52% of total variance); loose material type: $\eta_{\text{mat}}^2 = 0.363$ (36.3% of total variance); ligament width (a): $\eta_a^2 = 0.046$ (4.6% of total variance). The remaining variance (<8%) is attributed to factor interactions and residual numerical scatter.

These results quantitatively demonstrate that plate thickness is the dominant factor governing the averaged stress level, followed by the properties of the loose material, which control the effective distributed pressure and frictional interaction with the sieve. The ligament width, while clearly influential in controlled geometric comparisons (Figure 6), contributes a smaller share to the global variance when thickness and material effects are simultaneously present. This hierarchy is fully consistent with plate bending theory and FEM-based sensitivity studies, where thickness directly scales bending stiffness, whereas material properties scale the applied load magnitude.

Figure 9 presents three service life curves, which correspond to epicycloidal hole geometries with $k = 5$, $k = 7$, and $k = 9$, respectively, and demonstrates the capability of the proposed methodology to quantitatively predict sieve durability.

For granite, the intersection of the experimentally measured wear curve with the FEM-predicted critical thickness yields a service life of approximately 5790 h for $k = 5$ (SL-3), 4090 h for $k = 7$ (SL-2), and 3180 h for $k = 9$ (SL-1), indicating a systematic reduction of operational life with increasing epicycloid module. Thus, Figure 9 provides a direct and physically grounded validation of the proposed approach, in which the coupling of experimental wear kinetics with numerically determined critical thickness enables reliable, geometry-dependent forecasting of the service life of perforated sifting plates.

The proposed methodology and analysis of dependencies (Figure 9) allowed us to establish

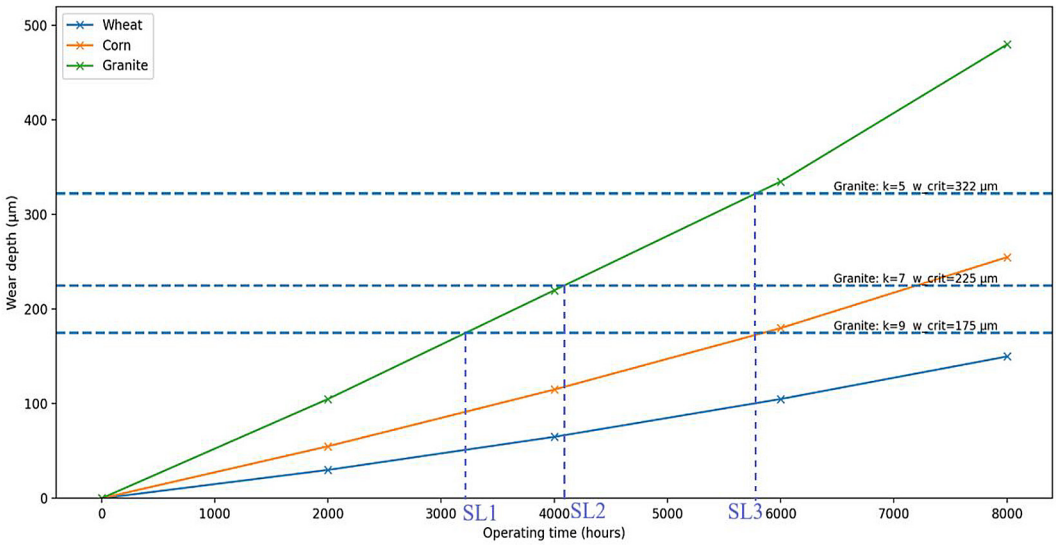

Figure 9. Wear dependence of the perforated plate thickness over operating time

Table 8. Critical thickness of the perforated plate s_{crit} (at σ = 235 MPa)

Loose material	Critical thickness of the perforated plate, mm		
	Epicycloidal holes k = 5	Epicycloidal holes k = 7	Epicycloidal holes k = 9
Wheat	0.4148	0.5747	0.6293
Corn	0.2193	0.4264	0.4940
Granite	0.6776	0.7749	0.8252

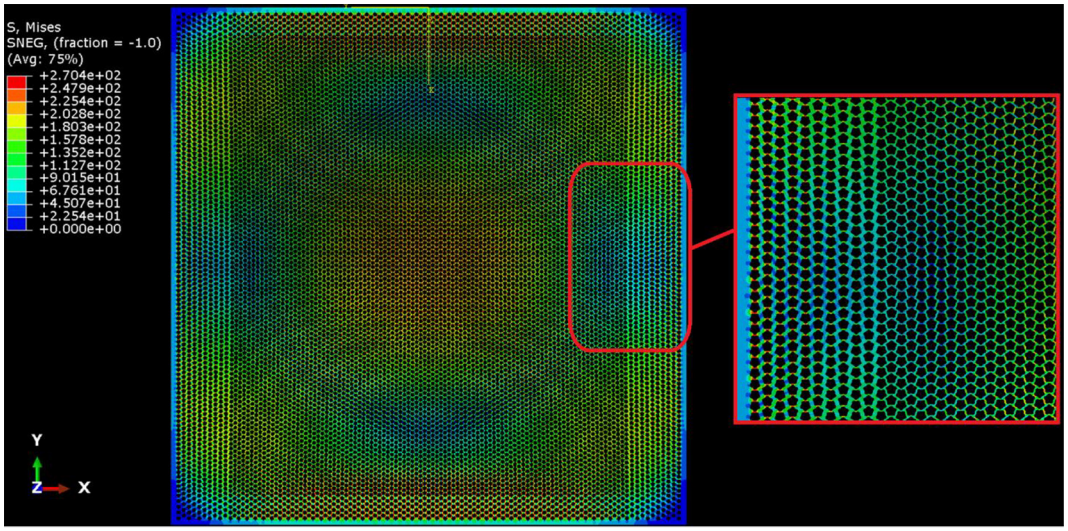

Figure 10. Example of increased stiffness in the perforated plate by enlarging ligament width in zone A (loose material – granite, plate size 1 × 1 m, epicycloid hole k = 5, s = 0.6 mm)

critical values of the thickness of the perforated plate for three loose materials and three types of epicycloidal holes (k = 5, 7, 9). In the present study, the strength threshold used for defining the critical thickness s_{crit} and the service-life curves is taken as the allowable stress (Equation 1). For the service-life mapping in Figure 9 and the corresponding critical thickness values in Table 8, n = 1 was used to relate the FEM-predicted stress state directly to the onset of yielding under the assumed material model. The data obtained (Table 8) indicate a critical proximity to the yield strength of the plate material (specified steel), which allows predicting the service life of perforated plates with complex geometry holes based on operating time (for example, in the form of an illustrative diagram, Figure 9).

Table 9. Comparison of stresses in perforated plates (loose material – granite, plate size 1 × 1 m, epicycloidal hole $k = 5$, $s = 0.6$ mm)

Plate thickness *s*, mm	Ligament width *a*, mm		Averaged stresses in the zone *A* $\bar{\sigma}_{vM}$, MPa	Averaged stresses in the zone *B* $\bar{\sigma}_{BvM}$, MPa
	zone *A*	zone *B*		
0.6	1	1	282.7	101
	1.5	1	266.35	95.15
1	1	1	102.6	36.7
	1.5	1	95.8	34.2

One possible solution is to increase the stiffness of the perforated plate structure in the identified critical zones. For example, a study was conducted on stress reduction in the peripheral zones by increasing the width of ligaments (distance between holes) in corresponding rows (Figure 10, Table 9).

The results in Table 9 demonstrate that a local increase of ligament width from 1.0 to 1.5 mm in the peripheral rows leads to a systematic reduction of peak stresses in the perforated plate. For granite at $s = 0.6$ mm, the maximum stresses decreased to 5.8% (from 282.7 to 266.35 MPa in zone *A*, and in zone *B* – from 101.0 to 95.15 MPa). A sim ilar trend was observed at $s = 1.0$ mm, where the reduction in stresses was up to 6.5%, confirming the stability of the effect. These results indicate that targeted reinforcement of peripheral ligaments represents an effective and technologically feasible design strategy to reduce local stress concentrations and thereby increase the durability and service life of perforated sifting plates without a significant increase in material consumption.

CONCLUSIONS

An integrated experimental–numerical framework was developed to predict the service life of perforated sifting plates with epicycloidal holes ($k = 5, 7, 9$) under real granular loading, explicitly coupling measured abrasive wear kinetics with FEM-based stress evaluation in critical zones *A* (periphery) and *B* (center).

Wear tests showed degradation that was highly dependent on the material: after 8000 hours, the loss of thickness reached 150 μm (wheat), 255 μm (corn), and 480 μm (granite), while the average wear rates were 0.02 μm/h, 0.03 μm/h, and 0.06 μm/h, respectively, confirming granite as the most aggressive environment for the strength of the perforated plate.

FEM revealed stable localization of critical stresses in two repeatable regions: Zone *A* (peripheral, clamped boundary) and Zone *B* (central). Under the most severe configuration ($a = 1$ mm, s = 0.6 mm, $k = 9$), the averaged stresses in Zone *A* were approximately 140–149% from Zone *B*, proving that service life is governed by the peripheral constraint zone.

The influence of significant factors on the magnitude of stresses in a perforated plate has been established. Thus, increasing the width of the bridge from $a = 1$ to 3 mm reduced the average stresses by ~22–23%, and an increase in thickness from $s = 0.6$ to 1.0 mm reduced the stress in the critical case (wheat, $k = 9$, zone *A*) by 61.6%, confirming the presence of thickness as the main level of rigidity against stress intensification during wear processes. An increase in the epicycloidal modulus from $k = 5$ to $k = 9$ increased the average stress in zone *A* by ~49.5% for wheat, while for granite, the same configuration reached 422.6 MPa, which is 80% higher than the permissible stress (235 MPa), indicating a high probability of transition to an elastic-plastic mode under severe operating conditions.

Using the full factorial dataset (27 FEM cases, Zone *A*, $k = 9$), ANOVA effect sizes quantified the dominance of plate thickness ($\eta^2 = 0.520$) and loose material type ($\eta^2 = 0.363$) over ligament width ($\eta^2 = 0.046$), while the remaining variance (<8%) was attributed to interactions and residual scatter—providing a statistically grounded ranking consistent with plate bending mechanics and load scaling.

Critical residual thickness values at the yield criterion $\sigma = 235$ MPa were established for all materials and hole types (e.g., granite: $s_{crit} = 0.6776/0.7749/0.8252$ mm for $k = 5/7/9$), enabling life prediction by mapping experimental wear curves to FEM-based strength limits; additionally, a practical reinforcement strategy, locally increasing peripheral ligament width from 1.0 to 1.5 mm, reduced peak stresses by ~5.8% ($s = 0.6$ mm) and ~6.5% ($s = 1.0$ mm), demonstrating a feasible route to extend service life with minimal added material.

Acknowledgments

The authors acknowledge the financial support of the National Science Centre in Krakow to the research project funded in the „POLONEZ BIS 2" call No. 2022/45/P/ST8/02312 entitled Numerical-experimental analysis of a sieve holes' shape and arrangement effect on the degree. POLONEZ BIS is operated by the Centre on the basis of the Grant Agreement No. 945339 concluded with the European Research Executive Agency.

REFERENCES

1. Atanasiu C, Sorohan Ş. Displacements and stresses in bending of circular perforated plate. IOP Conference Series: Materials Science and Engineering 2016, 147: 012095. https//doi.org/10.1088/1757-899X/147/1/012095
2. Chen Z, Tong X, Li Z. Numerical investigation on the sieving performance of elliptical vibrating screen. Processes 2020, 8: 1151. https://doi.org/10.3390/pr8091151
3. Piven M. Justification of grain mixture separation process by flat vibrating sieves. MOTROL. Comission of Motorization and Energetics in Agriculture 2015, 17(7): 163–169.
4. Kharchenko S, Kovalyshyn S, Zavgorodniy A, Kharchenko F, Mikhaylov Y. Effective sifting of flat seeds through sieve. INMATEH-Agricultural Engineering 2019, 58(2): 17–26. https//doi.org/10.35633/INMATEH-58-02
5. Bredykhin V, et al. Improving efficiency of corn seed separation and calibration process. Agricultural Engineering, Sciendo 2023, 27(1): 241–253. https://doi.org/10.2478/agriceng-2023-0018
6. Bakum M, Kharchenko S, Kovalyshyn S, Krekot M, Kharchenko F, Shvets O, Kiełbasa P, Miernik A. Identification of parameters of the separation process of safflower seed material on sieves. Journal of Physics: Conference Series 2022, 2408: 012013. https//doi.org/10.1088/1742-6596/2408/1/012013
7. Senjanović I, Hadžić N, Vladimir N. Vibration analysis of thin circular plates with multiple openings by the assumed mode method. Proceedings of the Institution of Mechanical Engineers Part M: Journal of Engineering for the Maritime Environment, 2017, 231(1): 70–85.
8. Dinkar MK. Vibration Analysis of Perforated Plates. Ph.D thesis, Birla Institute of Technology and Science, Pilani. 2015.
9. Folias E, Wang J. On the 3-dimensionl stress field around a circular holes in a plate of arbitrary thickness. Comput Mech, 1990, 6(3): 379–391.
10. Chai B. Free vibration of laminated plates with a central circular hole. Compos Struct, 1996, 35: 357–368.
11. Saraçoğlu MH, Uslu F, Albayrak U. Stress and displacement analysis of perforated circular plates. Challenge journal of structural mechanics, 2020, 6(3): 150–159. https://doi.org/10.20528/cjsmec.2020.03.006
12. Kharchenko S, Samborski S, Kharchenko F, Mitura A, Paśnik J, Korzec I. Identification of the natural frequencies of oscillations of perforated vibrosurfaces with holes of complex geometry. Materials 2023; 16: 5735. https//doi.org/10.3390/ ma16175735
13. Kharchenko S, Samborski S, Kharchenko F, Paśnik J. Numerical study of the natural oscillations of perforated vibrating surfaces with holes of complex geometry. Advances in Science and Technology Research Journal. 2023; 17(6): 73–87. https://doi.org/10.12913/22998624/174062
14. Civalek Ö, Çatal H. Linear static and vibration analysis of circular and annular plates by the harmonic differential quadrature (HDQ) method. Journal of Engineering and Architecture Faculty of Eskişehir Osmangazi University, 2003, XVII(1): 43–71.
15. Lee WM, Chen JT. Free vibration analysis of a circular plate with multiple circular holes by using indirect BIEM and addition theorem. Journal of Applied Mechanics, Transactions ASME, 2011, 78(1): 0110151–510.
16. Kharchenko S, Kharchenko F, Samborski S, Paśnik J, Kovalyshyn S, Sirovitskiy K. Influence of physical and constructive parameters on durability of sieves of grain cleaning machines. Advances in Science and Technology Research Journal. 2022, 16(6): 156–165. https://doi.org/10.12913/22998624/156128.
17. Timoshenko S, Woinowsky-Krieger S. Theory of Plates and Shells. McGraw-Hill Inc. 1959.
18. Jafari A, Saljooghi Nezhad V. Employing DEM to study the impact of different parameters on the screening efficiency and mesh wear. Powder Technology, 2016, 297: 126–143. https://doi.org/10.1016/j.powtec.2016.04.008.
19. Gierz Ł, Kruszelniacka W, Robakowska M, Przybył K, Koszela K, Marciniek A, Zwiachel T. Optimization of the sowing unit of a piezoelectrical sensor chamber with the use of grain motion modeling by means of the discrete element method. Case study: rape seed. Applied Sciences, 2022, 12(3): 1594.
20. Kruszelnicka W, Diviš J, Hlosta J, Gierz ŁA, Žurovec D. Calibration of selected bulk biomaterials parameters for dem simulation of comminution process. Case study: Corn and rice grains. Advances in Science and Technology Research Journal. 2022, 16(5): 64–77. https://doi.org/10.12913/22998624/152990
21. Azelmad E, Salmi A, Kennassi E, Bousshine L. Elastoplastic behavior analysis of clamped circular perforated thin plates. IOSR Journal of Mechanical and Civil Engineering 2018, 15(2): 23–37.
22. Konieczny MM, Achtelik H, Gasiak G. Finite element analysis (FEA) and experimental stress

analysis in circular perforated plates loaded with concentrated force. Frattura ed Integrita Strutturale 2020, 14(51): 164–173.

23. Achtelic H, Gasiak G, Grzelak J. Strength tests of axially symmetric perforated plates for chemical reactors: Part 2-Experiments. International Journal of Pressure Vessels and Piping, 2008, 85: 257–264.
24. Li Q, Huang W, Sanchez J, Wang P, Ding Q, Wang J. Free vibration analysis of rectangular plate with cutouts under elastic boundary conditions in independent coordinate coupling method. Computer Modeling in Engineering & Sciences, 2022, 134: 2093–2121. https://doi.org/10.32604/cmes.2022.021340.
25. Huang M, Sakiyama T. Free vibration analysis of rectangular plates with variously shape-holes. J Sound Vib, 1999, 226: 769–786.
26. Karakaya C. Numerical investigation on perforated sheet metals under tension loading. Open Chemistry, 2022, 20: 244–253, https://doi.org/10.1515/chem-2022-0142.
27. Saraçoğlu M, Uslu F, Albayrak U. Investigation of hole shape effect on static analysis of perforated plates with staggered holes. Int J Eng Innovative Res. 2021, 3(2): 133–44. https://doi.org/10.47933/ijeir.883510.
28. Boyko A, Fedchenko Z. Analysis of work conditions and causes wear holes separating sieves in service. Academic Journal. Series: Industrial Machine Building, Civil Engineering 2017, 1(48): 34–40.
29. Keen B, Haines W. On the effect of wear on small mesh wire sieves. The Journal of Agricultural Science. 1923, 13(4): 467–482, https://doi.org/10.1017/S0021859600003865
30. Varga M, Widder L, Griesinger M, Adam K, Badisch E. Wear progress and mechanisms in high temperature sieves, Engineering Failure Analysis, 2016, 61: 46–53. https://doi.org/10.1016/j.engfailanal.2015.07.032
31. Kharchenko S, Samborski S, Paśnik J, Kharchenko F. The natural oscillations of perforated sifting surfaces with epicycloidal holes. Advances in Science and Technology Research Journal. 2025, 19(1): 256–268, https://doi.org/10.12913/22998624/195463
32. Hutchings I.M. Tribology: Friction and Wear of Engineering Materials. Elsevier, United Kingdom (1992).
33. Blatnický M, Dižo J, Barta D, Droździel P. Engineering design and strength analyses of main load-bearing parts of a mechanical rack system. Diagnostyka, 2018, 19(4): 97–104.
34. Gierz Ł, Al-Sammarraie M. A. J., Özbek O, Markowski P. The use of image analysis to study the effect of moisture content on the physical properties of grains. Scientific Reports, 2024, 14(1): 11673.
35. Gierz Ł, Kolankowska E, Markowski P, Koszela K. Measurements and analysis of the physical properties of cereal seeds depending on their moisture content to improve the accuracy of DEM simulation. Applied Sciences, 2022, 12(2): 549.
36. Estrada Q, Zubrzycki J, Reynoso-Jardón E, et al. Numerical study of the energy absorption performance of 3D printed sandwich structures. Advances in Science and Technology Research Journal. 2023, 17(5): 153–162. https://doi.org/10.12913/22998624/171496.
37. Olshanskyi V, Olshanskyi S. Dynamics of a non-uniform grain layer on a flat vibrating sieve. Dynamical Systems, 2010, 28: 62–170.
38. Šťastniak P, Smetanka L, Droździel P. Computer aided simulation analysis for wear investigation of railway wheel running surface. Diagnostyka 2019, 20(3): 63–68.
39. Kharchenko S, Bilovod O, Lytvynenko V, Kelemesh A, Tarasenko D. (2024). Modeling the loading process of pneumatic separation channels. Technology Audit and Production Reserves 2024, 6(1(80): 16–24. https://doi.org/10.15587/2706-5448.2024.320265
40. Meneghetti G, Lazzarin P. Significance of the elastic peak stress evaluated by FE analyses at the point of singularity of sharp V-notched components. Fatigue & Fracture of Engineering Materials & Structures, 2007, 30: 95–106. https://doi.org/10.1111/j.1460-2695.2006.01084.x
41. Poutiainen I, Tanskanen P, Marquis G. Finite element methods for structural hot spot stress determination – a comparison of procedures, International Journal of Fatigue, 2004, 26(11):1147–1157. https://doi.org/10.1016/j.ijfatigue.2004.04.003
42. Mecséri B, Kövesdi B. Discussion on the hot-spot and notch stress based fatigue assessment methods based on test results. Int J Steel Struct, 2020, 20:1100–1114. https://doi.org/10.1007/s13296-020-00345-1.
43. Dassault Systèmes. Abaqus Analysis User's Guide (Version 6.14). Dassault Systèmes Simulia Corp. 2014.
44. Yang Z, Kim C-B, Cho C, Beom HG. The concentration of stress and strain in finite thickness elastic plate containing a circular hole, International Journal of Solids and Structures, 2008, 45(3–4): 713–731. https://doi.org/10.1016/j.ijsolstr.2007.08.030
45. You H, Zhang L, Lin X, Tang P and Du Q. Stress concentration characteristics and coefficient modification for DC04 steel with holes of finite thickness. Front. Mater. 2025, 12: 1692324. https://doi.org/10.3389/fmats.2025.1692324
46. van Keulen F, Haftka RT, Kim NH. Review of options for structural design sensitivity analysis. Part 1: Linear systems, Computer Methods in Applied Mechanics and Engineering, 2005, 194(30–33): 3213–3243. https://doi.org/10.1016/j.cma.2005.02.002
47. Kala Z, Valeš J. Sensitivity assessment and lateral-torsional buckling design of I-beams using solid finite elements, Journal of Constructional Steel Research, 2017, 139: 110–122. https://doi.org/10.1016/j.jcsr.2017.09.014